Lateral indentation of a thin elastic film

Miguel Trejo, Victor Romero, Eugenio Hamm, Enrique Cerda

Lateral Indentation of a Thin Elastic Film†

Miguel Trejo,[a] Victor Romero,[b] Eugenio Hamm[c] and Enrique Cerda[c]

Indentation is a standard, widely used technique in mechanical assays and theoretical analysis. It unveils the fundamental modes of deformation and predicts the response of the material under more complex loads. Here we present an experimental setup for testing thin-film materials by studying the lateral indentation of a narrow opening cut into a film, triggering a cascade of buckling events. The force response F is dominated by bending and stretching effects for small displacements and slowly varies with indenter displacement $F \sim d^{2/5}$, to finally reach a wrinkled state that results in a robust nonlinear asymptotic relation, $F \sim d^4$. Experiments with films of various thicknesses and material properties, and numerical simulations confirm our analysis and help to define an order parameter that accounts for the different response regimes observed in experiments and simulations.

1 Introduction

Since the first determination of the material properties in monolayer graphene by indentation[1], several studies have further developed this method to evaluate extremely soft materials under different boundary conditions and loads. Examples include the indentation of freestanding film[2,3], floating film[4,5], and pressurized shell[6–8]. In contrast with the response of a large, thick solid material, indentation deforms film or shell into complex topographies such as localized out-of-plane displacement, wrinkling, or folding, which shows the importance of the coupling between geometry and material properties.

Indentation is usually understood as a load applied in the direction normal to the film plane. Here we ask what would happen if the film were indented not transversally but along the lateral or in-plane direction as visualized in Fig. 1(a). This rather unfamiliar indentation configuration is however relevant in a number of tearing experiments that have been reported in the literature. Examples include the oscillating crack[9–11] that results when a blunt tool is drawn along a sheet with an initial slit and *concertina* tearing[12–14], which is obtained by drawing a tool along a ductile sheet. In perforated sheets where geometry transforms transversal indentation into lateral indentation, petalling crack patterns[15], spiral cracks[16], and intertwined spiral cracks[17] have been observed. These previous studies on tearing propose various conflicting scaling laws for the elastic energy stored while indenting but are entirely consistent with observed fracture patterns. The diverse scaling laws obtained experimentally are a sign of rich behavior before fracturing and must account for different mechanisms to store elastic energy in the film.

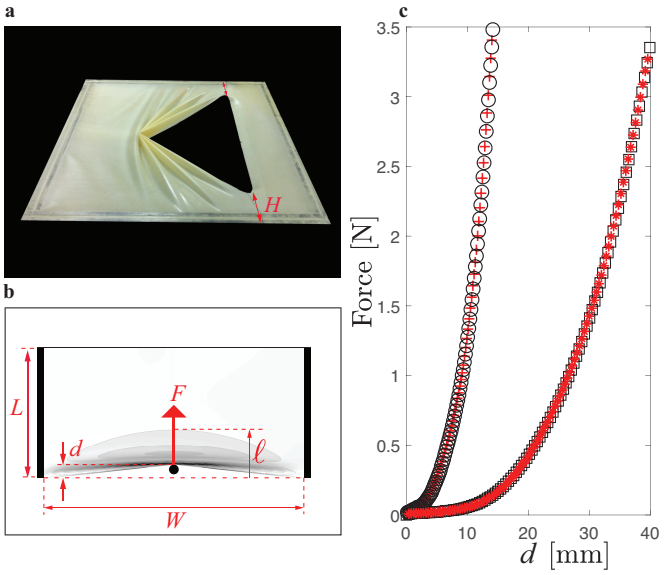

Fig. 1 (a) In-plane (pushing) forcing of a latex membrane fixed to a 50×50 cm^2 frame (see Supplementary Video 1†). The pushing tool is hidden by the wrinkles. (b) Experimental configuration for $H = 0$: the film is clamped on its lateral edges of length L (shown in black) and a rigid tool pushes at the middle of one of its free edges of length W. Measured quantities are F and d. The distance $\ell \geq d$ defines the penetration of the deformation into the film (see Supplementary Video 2†). (c) Force versus displacement for biaxially oriented polypropylene for $t = 30\,\mu$m and different setup configurations. Experiments for a slit ($W = 10$ cm) far from the clamped boundaries (open squares) are indistinguishable from experiments ($*$) where the ends of the slit coincide with the system boundary ($H = 0$). Similarly, experiments ($W = 50$ cm) for indenters of diameter 5 mm (open circles) and 10 mm ($+$) give the same equivalent force-displacement response. Numerical simulations confirm the weak dependence on these parameters (see ESI† for more details).

Inspired by these previous experiments, we study herein the lateral indentation of a free boundary made in a film by cutting a narrow opening of length W [see Figs. 1(a), and 1(b), and the Supplementary Videos†]. Before the cracks at the end of the cut start to grow, the indented film bends out-of-plane first forming a

[a] *Instituto de Física de Buenos Aires (IFIBA-CONICET), Departamento de Física, Facultad de Ciencias Exactas y Naturales, Universidad de Buenos Aires, Ciudad Universitaria, Buenos Aires, Argentina.*

[b] *Univ. Grenoble Alpes, Inria, CNRS, Grenoble INP, LJK, Grenoble, France.*

[c] *Universidad de Santiago de Chile (USACH), Facultad de Ciencia, Departamento de Física, Chile; E-mail: enrique.cerda@usach.cl*

† Electronic Supplementary Information (ESI) available: Three supplementary videos are provided to help understand the experimental and numerical setup. Videos 1 and 2 (speeded up 4x) show experiments for LATEX ($W = 0.4$ m, $t = 100\,\mu$m) and B0PP1 ($W = 0.2$ m, $t = 50\,\mu$m), respectively. Video 3 shows a numerical simulation in Abaqus for $W = 0.2$ m and $t = 0.5\,\mu$m. We also provide a detailed description of the numerical method implemented in the Abaqus solver (ESI section II), the study of the sensitivity to other physical parameters (ESI section III), the buckling analysis of the system (ESI section IV), and the study of the in-plane tension under near and far-from-threshold conditions (ESI section V). See DOI: 10.1039/D1SM01348C.

large fold connecting the indenter with the points where the edge is pinned; further indentation leads to a cascade of instabilities that wrinkles the surface. Here we show that the force response in this configuration is characterized by the penetration length, ℓ, along which the indenter deforms the film [see Fig. 1(b)] and the results are independent of (i) the specific boundary conditions far from the edge and (ii) the size of the indenter. Moreover, lateral indentation is highly sensitive to material properties and can be implemented as a measurement tool for thin films.

2 Experimental and Numerical Analysis

Figure 1(c) shows the result of two sets of force versus displacement experiments for bi-oriented polypropylene to study the effect of the indenter diameter and the distance from the cracks to the boundaries, H, where the film is clamped [see Fig. 1(a)] . Varying the indenter diameter or using a zero or finite distance H gives an equivalent response. Similar experiments done with films of various lengths $L \gtrsim W$ [see Fig. 1(b)] reveal a weak dependence on the aspect ratio of the film, or the specific boundary condition applied to the side opposite the indented edge (see ESI†). Given that the mechanical response does not depend on these conditions, we conclude that the only relevant length scales in the problem are the size W of the slit and the indenter displacement d. Moreover, we expect, based on dimensional grounds, that the force displacement relation for a pure elastic response is dictated by two-dimensionless parameters d/W and YW^2/B, where $B = Et^3/12(1-\nu^2)$ is the bending stiffness of the material, $Y = Et$ is the two-dimensional Young's modulus, E is the film modulus, ν is Poisson's ratio and t is the film thickness. The second dimensionless parameter can be written as $N \equiv (YW^2/B)^{1/2} = \sqrt{12(1-\nu^2)}W/t$ which is proportional to the von Kármán number W/t, implying a general force-displacement relation $F/(YW) = \Pi(d/W, N)$. A third dimensionless parameter is the yield strain ε_Y, which defines the strain deformation corresponding to the onset of nonlinear (plastic or elastic) material behavior [18]; however, this parameter is relevant only for large deformations.

Since the material response due to indentation depends strongly on the length of the edge, further experiments and simulations were performed with a film constrained at two boundaries ($H = 0$) and with the indenter applied to one of the remaining free boundaries [see Fig. 1(b)]. Figure 2(a) shows a log-log plot of the dimensionless force F/YW versus the dimensionless displacement d/W for rubber latex (LATEX, $E = 0.24$ GPa, $\nu \approx 0.5$, $\varepsilon_Y = 0.2$), polydimethylsiloxane (PDMS, $E = 0.002$ GPa, $\nu \approx 0.5$, $\varepsilon_Y = 0.2$), aluminum foil (ALUM, $E = 32.4$ GPa, $\nu = 0.3$, $\varepsilon_Y = 0.03$), polyethylene (PET, $E = 5.5$ GPa, $\nu = 0.33$, $\varepsilon_Y = 0.08$), ultrathin polyester mylar film (OS, $E = 5.3$ GPa, $\nu = 0.4$, $\varepsilon_Y = 0.08$), and two different biaxially oriented polypropylene films (BOPP1, $E = 2.6$ GPa, $\nu = 0.3$ and BOPP2, $E = 2.3$ GPa, $\nu = 0.33$, with $\varepsilon_Y = 0.08$ for both), with von Kármán numbers ranging from 25 to 4×10^5. All these material properties were obtained by testing rectangular samples in a traction machine (Instron). A large spread of the curves appears for small displacement reflecting the fact that films with larger von Kármán numbers require less force to be indented. However, when the films are highly wrinkled, the curves start to approach the asymptotic line $F \sim d^4$ for large displacement. This asymptotic behavior or stretching-dominated regime persists until the material reaches the strain ε_Y and the uniaxial response is no longer linear.

Material nonlinearities are explained by hyperelastic behavior in the case of LATEX and PDMS and by plastic deformation for the remaining materials in Fig. 2(a). The typical strain is estimated from the change in length of the edge due to pushing a distance d and equals $\sqrt{d^2 + (W/2)^2} - W/2$. The corresponding strain for $d \ll W$ is $\varepsilon \approx 2(d/W)^2$, which gives an upper bound for indentation $d/W < (\varepsilon_Y/2)^{1/2}$ under which the system is linear and reversible. The transition from a regime dominated by bending effects to a regime dominated by stretching takes place at a lower value of indentation for thinner films and, consequently, the response $F \sim d^4$ occurs over a wider window of displacement.

This qualitative description is confirmed by numerical simulations in Abaqus by using a combination of the dynamic explicit and static solvers to search for the solutions. Additionally, the numerical analysis allows for studying the pure elastic response of the material and provides a better understanding of the force-displacement response for thinner films where dynamic effects and experimental error become important. Considering that various metastable solutions are compatible with the applied boundary conditions and loads, we first used the explicit solver because of its efficiency for searching low-energy solutions in thin films. Given that the deformation is dominated by stretching for large indentation and thinner films, the force-displacement relation must have the dimensionless form $F/(YW) = \Pi(d/W)$ in that limit. Under these conditions, we used the numerical results to fit the experiments for the thinnest of our films (OS film, $t = 0.5$ μm) by using stretching modulus Y as fitting parameter (for more details, see ESI†). The result is $E \approx 5.7$ GPa. We independently measured $E \approx 5.3$ GPa in a standard uniaxial traction experiment. The good agreement shows that we are numerically tracking the minimal-energy solution compatible with the imposed constraints. Once it is established that we are studying the solutions with minimal global energy for large indentation, we shift backwards from large to small indentation by combining the static and dynamic implicit solvers to track the minimal global solution in the bending-dominated regime. In this manner, we also observe numerically the compressive force-displacement relation before buckling, as shown in Fig. 2(b) (solid black line).

3 Far From Threshold Analysis

The transition from a bending-dominated regime to a regime where the sheet is highly wrinkled and the dominant energy comes from stretching is consistent with the near-threshold (NT) to far-from-threshold (FT) transition studied in previous works under different load configurations [20,21]. To characterize the FT regime, we assume that the tensional lines of the wrinkled part are in the radial direction starting from the ends of the free edge and making an angle θ with respect to the edge. In Fig. 3 we focused on the left side of the film so that the end of the edge is at $(x, y) = (0, 0)$ and

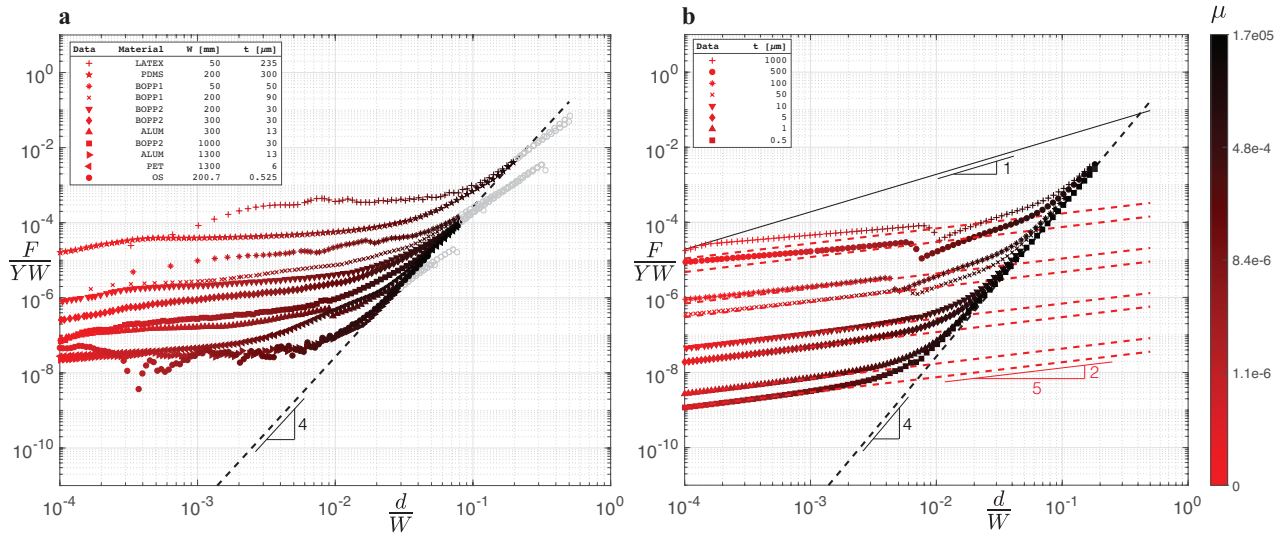

Fig. 2 (a) Force versus displacement in experiments using films of various materials. For each film, N increases as the corresponding data set moves from top to bottom. Data points above $\varepsilon > \varepsilon_Y$ are shown in gray. The color map from light to dark red is proportional to the bendability parameter $\mu = (8/3)(d/W)^{18/5}N^{6/5}$ defined in the main text. (b) The equivalent numerical simulations in Abaqus for an elastic film ($E = 4.4$ GPa, $\nu = 0.4$, $W = 0.2$ m) with varying film thickness. The solid black line illustrates the initial compressive response for the thickest film ($t = 1$ mm) and scales linearly, $F \sim Yd$. The dashed black line in both figures corresponds to Eq. (3) and the red dashed lines in panel (b) show, for each film, the scaling law (4) describing the near-threshold regime.

the indenter is applied at position $(x,y) = (W/2, 0)$. Because the FT regime assumes a vanishing stress transversal to the wrinkles, we assume $\sigma_{\theta\theta} = \sigma_{r\theta} = 0$ in the following. We conclude from force balance along the radial direction, $\partial_r(r\sigma_{rr}) - \sigma_{\theta\theta} + \partial_\theta \sigma_{r\theta} = 0$, that the radial stress compatible with equilibrium must have the form $\sigma_{rr} = C(\theta)/r$. Because the film is under uniaxial tension, we expect a stress-displacement relation of the form $\sigma_{rr} = Y\partial_r u_r$ where u_r is the displacement in the radial direction. Integration gives $u_r = C(\theta)\ln(r) + D(\theta)$, where C and D are obtained from the conditions imposed by the indenter. Points along the center of the film at an initial position $r_i = W/(2\cos\theta)$ move to the new position $r_f = W/(2\cos\theta_f)$, where $\theta_f \approx 2d/W$ is the final angle after displacement (see Fig. 3). As a result, we enforce $u_r|_{r_i} = r_f - r_i$.

A second boundary condition is obtained by assuming zero displacement for $r = 0$; however, the singular behavior of the solution at this position implies that our solution is no longer valid for $r < r_*$, where r_* defines the size of the singularity. Therefore, we apply the boundary condition $u_r|_{r_*} = u_*$ and assume that u_* is much smaller than $r_f - r_i$. The resulting radial stress is

$$\sigma_{rr} = \frac{YW\eta}{4}\frac{(\theta_f^2 - \theta^2)}{r}, \tag{1}$$

where $\eta = 1/\ln(r_i/r_*)$ is a slowly varying parameter that we assume to be constant in the following. A similar logarithmic parameter is obtained when one or both principal stresses in a problem of elasticity follows the scaling law $\sim 1/r$ since a different physical regime must remove the singularity in the stress. Examples are the stresses around a 2D dislocation[22] or bending stresses in 3D conical deformations[23].

The force on an arc element is given by $(\sigma_{rr} r d\theta)\hat{r}$, where $\hat{r} = \hat{x}\cos\theta + \hat{y}\sin\theta$ is a unitary radial vector in the original undeformed film. However, because of the large rotation of the tension lines in the strongly deformed film, the unitary vector $\hat{r}$ rotates to $\hat{r}_f = \hat{x}\cos\theta_f + \hat{y}\sin\theta_f$ to follow the position of the indenter (see Fig. 3). We conclude that the force on the arc element is now $(\sigma_{rr} r d\theta)\hat{r}_f$.

To connect the tensional model with our experiments, we used the traction vector per unit length, $\vec{f}(\hat{n})$, where $\hat{n}$ is the orientation of the length element. This force is given in terms of the stress tensor in two dimensions by the relation $f_i(\hat{n}) = \sigma_{ij} n_j$. For equilibrium balance, the force along the center line is such that $\vec{f}(\hat{x})dy = (\sigma_{rr} r_i d\theta)\hat{r}_f - (\sigma_{\theta\theta} dr)\hat{\theta}_f$, where $\hat{\theta}_f$ is orthogonal to $\hat{r}_f$. Because $\sigma_{\theta\theta} = 0$ and $dy\cos\theta = r_i d\theta$, we obtain $\vec{f}(\hat{x}) = (\sigma_{rr}\cos\theta)\hat{r}_f$. With the previous definitions we can now compute the exerted force as[24]

$$F = 2\int_0^d dy \vec{f}(\hat{x})\cdot\hat{y}. \tag{2}$$

Here the factor of two accounts for the contributions from both sides of the film. Replacing the expression for the force $\vec{f}$, we obtain $F = 2\sin\theta_f \int_0^d dy\cos\theta\sigma_{rr}|_{r=r_i} = Y\eta\sin\theta_f \int_0^d dy\cos^2\theta(\theta_f^2 - \theta^2)$, which, for small angles $\theta \approx 2y/W$, gives

$$\frac{F}{YW} = \frac{16}{3}\eta\left(\frac{d}{W}\right)^4. \tag{3}$$

This relation is represented as a black dashed line in Fig. 2 and the best fit of the numerical simulation for large displacements gives the value $\eta \approx 0.5$. We conjecture that a better description of the deformation near the clamped edges should account for this simple value.

4 Near Threshold Analysis

The response $F \sim d^4$ was anticipated by Audoly et al.[9] by assuming a total stored energy $U \sim Y\varepsilon^2 S$, where S is the stretched area. The constitutive relation $F = \partial_d U$ implies $F \sim d^4$ if the stretched area

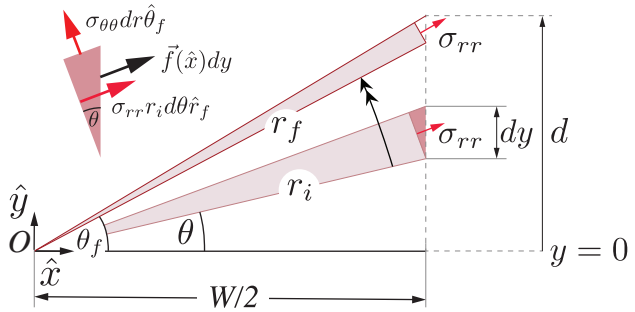

Fig. 3 Geometry of tensional model. Only one half of the membrane is represented. Pushing up to $y = d$ collapses all material points lying on the dashed vertical line. A material radial line of length r_i stretches to line r_f so that lines closer to the edge are more stretched. The expanded view shows the balance of forces at the center line $\vec{f}(\hat{x})dy = (\sigma_{rr} r_i d\theta)\hat{r}_f - (\sigma_{\theta\theta} dr)\hat{\theta}_f$ after they are moved to the point $y = d$.

is estimated as $S \sim dW$. Thus, the penetration length ℓ of the deformation coincides with the indenter displacement, or $\ell \approx d$. This hypothesis was challenged in subsequent work in which it was observed that small indentations produce deformations at distances larger than d. In fact, Vermorel et al.[15] assumed $\ell \approx W$ and Tallinen et al.[14] estimated $\ell \approx \lambda$ where λ is the size of the large initial fold detected while indenting. We show below that these different estimations for the penetration length are observed; however, they are correct in different regions of the force-displacement response because ℓ is a complex function of the indenter displacement.

The classical buckling analysis for an infinite strip clamped at its two parallel boundaries[25] shows that the buckling force per unit length is $F_c/W \approx B/W^2$, which must be compared with the buckling force of a rectangular film of width W and length ℓ, which is $F_c/W \approx B/\ell^2$. This implies that the initial penetration distance of the deformation in our configuration is $\ell \approx W$. Additionally, the analysis of the pure in-plane compression before buckling leads to the relation $F \approx Yd$ [see Fig. 2(b)] and predicts a critical displacement for buckling of $d_c/W \approx 1/N^2$, which is much less than the penetration length. The critical displacement is typically in the range of a few microns for the thicker films in the experiments of Fig. 2(a) and was difficult to detect because of the limitations of our setup. In ESI†, we provide a more precise numerical description of the behavior near the buckling conditions.

After buckling, the first fold of wavelength λ emerges (see Supplementary Video 2†), stiffening the system since the penetration length is given by $\ell \approx \lambda < W$, which predicts a larger force $F/W \approx B/\lambda^2$ for this post-buckling regime. To understand the emergence of this first fold, we follow the description of Tallinen and Mahadevan[14] who report a similar precursor wavelength λ in numerically simulated *concertina* tearing. The initial indentation generates a fold of amplitude A that, for inextensibility[19], must be related to the indenter displacement by $A \approx \sqrt{\lambda d}$. As opposed to the in-plane stretching $\varepsilon \approx 2(d/W)^2$ caused by the indenter, this amplitude deformation produces out-of-plane stretching $\varepsilon_A \approx (A/W)^2$. Thus, we obtain $\varepsilon/\varepsilon_A \approx d/\lambda$, which shows that $\varepsilon \ll \varepsilon_A$ for $d \ll \lambda$ or small indentation.

To account for the wavelength, we use the balance to explain tensional wrinkling: $\lambda \approx (B/T)^{1/4} W^{1/2}$, where T is the tension per unit length along the wrinkles[19–21]. However, in our configuration, the tension is not an independent parameter but is given by the largest strain $T \approx Y\varepsilon_A$, which is a function of amplitude and wavelength. Solving the previous relations for the amplitude and wavelength, we obtain $\lambda/W \sim N^{-2/5}(d/W)^{-1/5}$ and $A/W \sim N^{-1/5}(d/W)^{2/5}$. The maximum wavelength occurs at the critical displacement for buckling ($d_c/W \approx N^{-2}$), which yields $\lambda \approx W$ and connects this bending-dominated regime to the analysis for buckling.

Similarly, the indentation force in this post-buckling regime is $F/W \sim B/\lambda^2$, or, equivalently,

$$\frac{F}{YW} \approx c N^{-6/5} \left(\frac{d}{W}\right)^{2/5}, \tag{4}$$

where c is a constant. Figure 2(b) shows that this fit precedes the FT regime and explains the data after buckling. We obtain $c \approx 1$ as the best fit for the numerical data in Fig. 2(b) and the thinnest film. Similarly, Fig. 4 shows the collapse of the experimental data for small displacements when using the dimensionless variables defined by Eq. (4). Parameter c has a weak dependence on the contact conditions between indenter and film or the specific boundary conditions used in the simulations (see ESI†). This is explained by the sensitivity of the buckling force to specific boundary conditions and load distribution, and the necessary matching that must occur between Eq. (4) and the buckling force $F_c/(YW) \approx 1/N^2$ at $d = d_c$.

The tension and wrinkling behaviors observed under FT conditions differ completely. For $\lambda \ll d$, the penetration length is $\ell \approx d$; thus, the in-plane strain dominates and the tension compatible with Eq. (3) is predicted to be $T \approx Y\varepsilon$. Again using the balance $\lambda \approx (B/T)^{1/4} W^{1/2}$ leads to a scaling for the wavelength of $\lambda/W \sim N^{-1/2}(d/W)^{-1/2}$. Thus, the wavelength becomes more sensitive to indentation in the FT regime. Here, the buckling force estimated as $F/W \approx B/\lambda^2$ is overcome by the force obtained by the pure tensional analysis of Eq. (3).

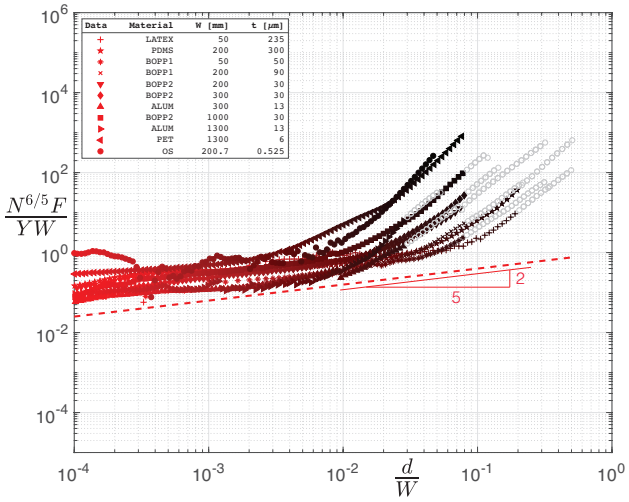

Fig. 4 Collapse of experimental data given in Fig. 2a (same color map) by using the dimensionless variables defined in Eq. (4). The red dashed line corresponds to Eq. (4) for $c \approx 1$.

A key element to understand the different scaling laws for the

wavelength is the in-plane tension T produced by the indenter. However, this is a spatially fluctuating variable that is difficult to track. A more robust variable, directly connected to the tension, is the total sectional force along the centerline of the film, $\tau = \int_0^\infty dy \vec{f}(\hat{x}) \cdot \hat{x} = \int_0^\infty dy \sigma_{xx}$. This force can be approximated as $\tau \sim T\ell$ because the tension is negligible at lengths greater than the penetration length. Using the previous results, we obtain $\tau/(YW) \approx T\lambda/(YW) \approx N^{-4/5}(d/W)^{3/5}$ in the NT regime, and $\tau/(YW) \approx Td/(YW) \approx (d/W)^3$ in the FT regime. Figure S7 in ESI† confirms these scalings.

The predicted indentation force for the NT and FT regimes naturally defines a bendability parameter as the ratio between relations (3) and (4): $\mu \equiv (8/3)[(d/W)^{3/5}N^{1/5}]^6$, giving the condition to be in a FT regime as $\mu \gg 1$. We use the bendability parameter to define the color map in Fig. 2 showing the behavior corresponding to the NT (light red) and FT (dark red) regimes. As in similar problems where these two regimes appear, the transition is not completely predicted by the von Kármán number. In fact, a nonzero displacement is required to satisfy the FT conditions, which are given by $\mu_* \approx 1$ or $(d/W)_* \approx (3/8)^{5/18}N^{-1/3}$. Note that $\lambda \approx d_*$ for this value of displacement by using the scaling law for wrinkling either in the NT or FT regime. This completes our description of the penetration length as a function of displacement. It moves from $\ell \approx W$ for $d_c/W \approx 1/N^2$ to smaller values following the scaling $\ell \approx \lambda \approx WN^{-2/5}(d/W)^{-1/5}$ for displacements in the range $d_c < d < d_*$ until the point where $\ell \approx d$ for $d = d_*$, beyond which the penetration length increases again following the scaling $\ell \approx d$.

5 Conclusions

The previous analysis can be summarized by the general relation

$$\frac{F}{YW} \approx cN^{-6/5}\left(\frac{d}{W}\right)^{2/5} + \eta\frac{16}{3}\left(\frac{d}{W}\right)^4 \quad (5)$$

which accounts for the two different behaviors observed. Equation (5) constitutes a new metrology tool to obtain the material properties of an extremely thin film in the same way that transversal indentation has been used to obtain the material properties of ultrathin films such as graphene [1] by using the classical Schwerin relation [2,26]. In contrast to the Schwerin relation where out-of-plane deformation is coupled with the necessary boundary conditions applied to restrain the film, lateral indentation deforms the film in a localized region defined by the slit size. Thus, while the relevant length scale in normal indentation is the system size, the relevant length scale in lateral indentation is the edge length W. This localized response agrees with previous tearing experiments [9–17] where boundary conditions far from the fracture propagation play no role.

The first term in Eq. (5) gives the bending stiffness of the film, and the second term gives the stretching stiffness of the material by fitting the experimental data. Although the force displacement relation for lateral indentation is clearly similar to that for transverse indentation, the loading configurations differ. Normal indentation easily puncture a film because the stresses at a distance r from the indenter are of order [2] $\sim 1/r^{2/3}$. Although the indenter dimensions cut off the singularity, its size must be calibrated to avoid reaching the strength of the film. In lateral indentation, the stress is distributed over a distance d so that greater forces can be applied to unveil the complete underlying stress-strain relation of the material.

The in-plane indentation configuration defines a highly sensitive system to study other effects such as tension or plastic effects. Since wrinkling under FT conditions corresponds to uniaxial traction in one principal direction, we can include in Eq. (5) the effective stress-strain response and explain the departure from the FT theory observed in Fig. 2 for $\varepsilon > \varepsilon_Y$. Similarly, initial prestress T_{pre} or tension imposed at the boundaries or free edge will remodel Eq. (5) when they dominate the inner tension T obtained for the NT and FT regime; hence, Eq. (5) is valid under the assumption $T \gg T_{\text{pre}}$ for a given displacement.

Conflicts of interest

There are no conflicts to declare.

Acknowledgements

E.C. acknowledges the support of Fondecyt Grant No 1201250. V.R. would like to thank ERC for support and grant GEM (StG-2014-639139). E.H. was funded by VRIDEI - DICYT project 041931HH and thanks the LIA-MSC sponsorship.

Notes and references

1 C. Lee, X. Wei, J.W. Kysar, and J. Hone, *Science* **321**, 385-388 (2008).

2 D. Vella and B. Davidovitch, *Soft Matter* **13**, 2264-2278 (2017).

3 R.D. Schulman and K. Dalnoki-Veress, *Phys. Rev. Lett.* **115**, 206101 (2015).

4 D.P. Holmes and A.J. Crosby, *Phys. Rev. Lett.* **105**, 038303 (2010).

5 D. Vella, J. Huang, N. Menon, T.P. Russell, and B. Davidovitch, *Phys. Rev. Lett.* **114**, 014301 (2015).

6 D. Vella, A. Ajdari, A. Vaziri, and A. Boudaoud, *Phys. Rev. Lett.* **107**, 174301 (2011).

7 D. Vella, A. Ajdari, A. Vaziri, and A. Boudaoud, *J. R. Soc. Interface* **9**, 448-455 (2012)

8 M. Taffetani and D. Vella, *Phil. Trans. R. Soc. A* **375**, 20160330 (2017).

9 B. Audoly, P.M. Reis, and B. Roman, *Phys. Rev. Lett.* **95**, 025502 (2005).

10 B. Roman, P.M. Reis, B. Audoly, S. De Villiers, V. Viguié, and D. Vallet, *C. R. Mecanique* **331**, 811-816 (2003).

11 P.M. Reis, A. Kumar, M.D. Shattuck, and B. Roman, *EPL* **82**, 64002 (2008).

12 A.G. Atkins, *Endeavour* **18**, 2-10 (1994).

13 A.G. Atkins, Science & Public Affairs. *Autumn*, 19-23 (1994).

14 T. Tallinen and L. Mahadevan, *Phys. Rev. Lett.* **107**, 245502 (2011).

15 R. Vermorel, N. Vandenberghe, and E. Villermaux, *Phys. Rev. Lett.* **104**, 175502 (2010).

16 V. Romero, B. Roman, E. Hamm, and E. Cerda, *Soft Matter* **9**, 8282-8288 (2013).

17 J.F. Fuentealba, E. Hamm, and B. Roman, *Phys. Rev. Lett.* **116**, 165501 (2016).

18 Strictly, yield strain defines the point where irreversible deformations become important; however, LATEX and PDMS do not yield but show a reversible nonlinear deformation at a critical strain. To simplify notation, we use ε_Y to mark the point where material and geometric nonlinearities change the linear stress-strain relation in a material.

19 E. Cerda and L. Mahadevan, *Phys. Rev. Lett.* **90**, 074302 (2003).

20 B. Davidovitch, R.D. Schroll, D. Vella, M. Adda-Bedia, and E. Cerda, *Proc. Natl. Acad. Sci. USA* **108**, 18227-18232 (2011).

21 B. Davidovitch, R.D. Schroll, and E. Cerda, *Phys. Rev. E* **85**, 066115 (2012).

22 J. Weertman and J.R. Weertman, *Elementary Dislocation Theory* (Oxford University Press, Oxford, 1992).

23 E. Cerda, S. Chaieb, F. Melo, and L. Mahadevan, *Nature* **401**, 46 (1999).

24 Equation (2) is equivalent to $F = 2\int \sigma_{xy}\, dy$, but $\sigma_{xy} = 0$ just in front of the indenter because of symmetry. Thus, the shear stress and force must be computed far from the indenter after the principal lines of force are rotated as shown in Fig. 3.

25 S.P. Timoshenko and J.M. Gere, *Theory of Elastic Stability* (McGraw-Hill, New York, 1988).

26 E. Schwerin, *Zeit. Angew. Math. Mech.* **9**, 482-483 (1929).